

SU(3) topological insulators in the honeycomb latticeU. Bornheimer,^{1,2,3} C. Miniatura,^{2,1,3,4,5,6} and B. Grémaud^{2,1,3,7,8}¹*Centre for Quantum Technologies, National University of Singapore, 3 Science Drive 2, 117543 Singapore*²*MajuLab, CNRS-UNS-SU-NUS-NTU International Joint Research Unit, UMI 3654, Singapore*³*Department of Physics, Faculty of Science, National University of Singapore, 2 Science Drive 3, 117551 Singapore*⁴*School of Physical and Mathematical Sciences, Nanyang Technological University, Singapore 637371, Singapore*⁵*Université Côte d'Azur, CNRS, InPhyNi, France*⁶*Institute of Advanced Studies, Nanyang Technological University, 60 Nanyang View, Singapore 639673, Singapore*⁷*Laboratoire Kastler-Brossel, Ecole Normale Supérieure CNRS, UPMC, 4 Place Jussieu, F-75005 Paris, France*⁸*Aix Marseille Université, Université de Toulon, CNRS, CPT, Marseille, France*

(Received 9 July 2018; published 12 October 2018)

We investigate realizations of topological insulators with spin-1 bosons loaded in a honeycomb optical lattice and subjected to a SU(3) spin-orbit coupling—a situation which can be realized experimentally using cold atomic gases. In this paper, we focus on the topological properties of the single-particle band structure, namely, Chern numbers (lattice with periodic boundary conditions) and edge states (lattice with strip geometry) and their connection to time-reversal symmetry and the sublattice symmetry. While SU(2) spin-orbit couplings always lead to time-reversal symmetric tight-binding models, and thereby to topologically trivial band structures, suitable SU(3) spin-orbit couplings can break time-reversal symmetry and lead to topologically nontrivial bulk band structures and to edge states in the strip geometry. In addition, we show that one can trigger a series of topological transitions (i.e., integer changes of the Chern numbers) that are specific to the geometry of the honeycomb lattice by varying a single parameter in the Hamiltonian.

DOI: [10.1103/PhysRevA.98.043614](https://doi.org/10.1103/PhysRevA.98.043614)**I. INTRODUCTION**

Over the last few years, the continuous progress in the degree of control, tunability, and flexibility of ultracold atomic gases experiments [1–3] has opened the laboratory door to a whole class of model Hamiltonians, as witnessed, for example, by the recent implementation of artificial gauge fields [4–10]. Some of these model Hamiltonians are directly inherited from condensed-matter physics, for instance, the integer and fractional quantum Hall effects [11–13]. More saliently, physicists have further proposed new theoretical ideas and physical situations, such as topological phases [14–19], non-Abelian particles [20], or mixed dimensional systems [21–25], that could be tested in the laboratory. In particular, experiments involving spinors, either made of bosons or fermions in different Zeeman sublevels, are now able to implement and study Abelian and non-Abelian gauge fields [17,26–29], even though the latter have not yet been implemented in a lattice geometry. In these systems, the kinetic energy term in the Hamiltonian allows for a modification of the internal degrees of freedom as the particle propagates [30,31], leading to a rich class of nontrivial physical phenomena, especially with interactions. In two-dimensional lattices, and in particular when spin-orbit coupling is present, the corresponding non-Abelian gauge fields induce nondiagonal hopping matrices in the tight-binding Hubbard Hamiltonian that mix and flip the spin degrees of freedom [30,31]. Two-component bosonic and fermionic gases (in the bulk or in a lattice) have been the subject of many recent analytical and numerical studies [32–46].

In marked contrast, three-component bosonic or fermionic gases subjected to a SU(3) gauge field have been much less studied: the experimental realization is more complicated [30,47,48] and their theoretical studies are more involved, the gauge field group being much larger [49–53]. On the other hand, tight-binding models with a SU(3) spin-orbit coupling can break time-reversal symmetry and lead to topological insulators: the bulk band structure is topologically nontrivial (nonzero Chern numbers) and edge states develop for a strip geometry [49]. Such a situation cannot occur in any kind of SU(2) models, as we will explain later. In addition, since SU(3) has a more complex group structure than SU(2), one expects a larger variety of spin textures for interacting particles. These spin textures are associated to different homotopy groups and appear both in the ground state and in the excitations above the ground state [19,50–54].

Our paper consists of three main parts. In Sec. II, we give some general properties of SU(N) tight-binding models and describe the SU(3) tight-binding model on the honeycomb lattice that we consider. In contrast to previous studies on similar systems [49,52], we especially focus on its time-reversal properties and the interplay with the unique band structure of the honeycomb lattice and its Berry curvature [55]. Consequently, we study the topological properties of the band structure obtained for a lattice with periodic boundary conditions and compute the corresponding Chern numbers [56–59] in Sec. III. Next we study the edge states that are expected in the lattice strip geometry, as inferred from the bulk-edge correspondence [60–64]. In Sec. IV, we show how to trigger a series of topological transitions in the band structure of our

SU(3) model (i.e., integer changes in the Chern numbers) by varying a single parameter in the Hamiltonian. The variety of such topological transitions is richer on the honeycomb lattice than on the square lattice. In Sec. V, we summarize our results and conclude with some perspectives.

II. SU(N) TIGHT-BINDING MODELS AND TIME-REVERSAL SYMMETRY

A. Some general properties

The general tight-binding Hamiltonian for noninteracting particles with spin s on a two-dimensional lattice has the following form:

$$\hat{H} = - \sum_{(i,j)} \hat{\psi}_i^\dagger T_{ij} \hat{\psi}_j, \quad (1)$$

where the sum is carried over all nearest-neighbor lattice site pairs $\langle i, j \rangle$ and where $\hat{\psi}_i^\dagger = (\hat{\psi}_{i,s}^\dagger, \dots, \hat{\psi}_{i,-s}^\dagger)$ is the $(2s + 1)$ -component row-spinor built at each lattice site i on the creation operators $\hat{\psi}_{i,\sigma}^\dagger$ for each spin component σ ($|\sigma| \leq s$). The $(2s + 1) \times (2s + 1)$ hopping matrix T_{ij} is connecting the different spin components at site j to the different spin components at site i . Since the Hamiltonian \hat{H} is Hermitian, one has $T_{ji} = T_{ij}^\dagger$. SU(N) tight-binding models ($N = 2s + 1$) are obtained with $T_{ij} = t_{ij} U_{ij}$, where t_{ij} are real positive numbers and where the matrices $U_{ij} \in SU(N)$ describe the unitary transformation of the spin states between sites j and i .

When the system is invariant under a certain discrete translation group \mathcal{T}_r , the spectrum of the Hamiltonian \hat{H} exhibits a band structure. Note that \mathcal{T}_r can differ from the Bravais translation group of the underlying lattice itself. (This is the case, for example, in the presence of an external magnetic field with rational flux per plaquette.) Each band n is described by its eigenvalues $\epsilon_n(\mathbf{k})$ and eigenvectors $|n, \mathbf{k}\rangle$ for all Bloch wave vectors \mathbf{k} in the first Brillouin zone BZ defined by the translation group \mathcal{T}_r . For an isolated band, one can define the first Chern number as [58,59,65,66]

$$C_n = \frac{1}{2\pi} \int_{BZ} d^2\mathbf{k} \Omega_n(\mathbf{k}), \quad (2)$$

where $\Omega_n(\mathbf{k})$ is the Berry curvature of the n th band,

$$\Omega_n(\mathbf{k}) = \left(\nabla_{\mathbf{k}} \times \underbrace{i \langle n, \mathbf{k} | \nabla_{\mathbf{k}} | n, \mathbf{k} \rangle}_{\mathbf{A}_n(\mathbf{k})} \right) \cdot \mathbf{e}_z, \quad (3)$$

and \mathbf{A}_n is the Berry connection of the n th band [58]. Being an integer, the Chern number can only change when two bands touch, that is, when a gap closes. Chern numbers of a given tight-binding Hamiltonian satisfy a ‘‘zero-sum rule’’: they all add up to zero. For inversion-symmetric systems (resp. for time-reversal invariant systems), it is well known that the Berry curvature is even (resp. odd) in the BZ :

$$\Omega_n(\mathbf{k}) = \begin{cases} +\Omega_n(-\mathbf{k}) & \text{inversion symmetry} \\ -\Omega_n(-\mathbf{k}) & \text{time reversal symmetry} \end{cases}$$

These two properties show that (i) the Berry curvature itself identically vanishes if \hat{H} is invariant under both space inversion and time reversal, and (ii) Chern numbers of time-reversal

invariant Hamiltonians are necessarily vanishing. Therefore, only systems that break time-reversal symmetry can have nontrivial topological properties, i.e., nonvanishing Chern numbers.

At the single-particle level, and up to an inessential overall phase factor, the (anti-unitary) time-reversal operator is defined as $\Theta = e^{-\frac{i\pi}{2} J_y} K$, where J_y is the projection of the spin operator \mathbf{J} of the particle on the y direction and where K is the complex conjugation operator. One has $\Theta^2 = \mathbb{1}$ for integer spins and $\Theta^2 = -\mathbb{1}$ for half-integer spins [67]. Under time reversal the tight-binding Hamiltonian becomes [68]

$$\Theta \hat{H} \Theta^{-1} = - \sum_{(i,j)} \hat{\psi}_i^\dagger \Theta T_{ij} \Theta^{-1} \hat{\psi}_j, \quad (4)$$

such that the topological properties of a tight-binding Hamiltonian \hat{H} depend crucially on the behavior of the different T_{ij} under time reversal. In particular, when the matrices T_{ij} are all *even* under time reversal, the corresponding tight-binding model is topologically trivial [65,66].

The hopping matrices T_{ij} can be expanded over the unit matrix and the $N^2 - 1$ (Hermitian) generators \mathcal{T}_n of the Lie algebra of SU(N),

$$T_{ij} = \tau_{ij}^{(0)} \mathbb{1} + i \sum_{n=1}^{N^2-1} \tau_{ij}^{(n)} \mathcal{T}_n. \quad (5)$$

The behavior of T_{ij} under time reversal can be directly inferred from that of the generators \mathcal{T}_n and the N^2 complex coefficients $\tau_{ij}^{(n)}$. For instance, for spin- $\frac{1}{2}$ systems, the generators of SU(2) are the Pauli matrices which are odd under time-reversal symmetry ($\Theta = -i\sigma_y K$). Therefore T_{ij} will be even under time reversal if and only if all coefficients $\tau_{ij}^{(n)}$ are real. As a result, for SU(2) tight-binding models, the hopping amplitudes are given by

$$T_{ij} = t_{ij} \exp[i\boldsymbol{\alpha} \cdot \boldsymbol{\sigma}] = t_{ij} \left(\cos \alpha \mathbb{1} + i \frac{\sin \alpha}{\alpha} \boldsymbol{\alpha} \cdot \boldsymbol{\sigma} \right), \quad (6)$$

where $\boldsymbol{\alpha}$ is a real vector and $\alpha = |\boldsymbol{\alpha}|$. This shows that SU(2) tight-binding models are invariant under time reversal and thereby topologically trivial.

On the contrary, for $N \geq 3$, that is for spins $s \geq 1$, the different generators have different behavior under time-reversal symmetry, allowing SU(N) tight-binding Hamiltonians to break this symmetry and to have a topologically nontrivial band structure. In this paper, we are considering a SU(3) system, i.e., spin-1 particles. In this case, the time-reversal operator is $\Theta = JK$ with

$$J = \begin{pmatrix} 0 & 0 & 1 \\ 0 & -1 & 0 \\ 1 & 0 & 0 \end{pmatrix}, \quad (7)$$

and the generators of the SU(3) group are the Gell-Mann matrices λ_a (see Appendix A). As explained above, the hopping amplitude can be written as $T_{ij} = \tau_{ij}^{(0)} \mathbb{1} + i \boldsymbol{\tau}_{ij} \cdot \boldsymbol{\lambda}$, where $\boldsymbol{\tau}_{ij}$ is an eight-component vector and $\boldsymbol{\lambda}$ the Gell-Mann vector made of the eight Gell-Mann matrices λ_a .

From the transformation properties of the Gell-Mann matrices under time reversal, T_{ij} can be split among the odd and the even sectors, $T_{ij} = \tau_{ij}^{(0)} \mathbb{1} + i \boldsymbol{\tau}_{ij}^{(o)} \cdot \boldsymbol{\lambda}^{(o)} + i \boldsymbol{\tau}_{ij}^{(e)} \cdot \boldsymbol{\lambda}^{(e)}$, such

that T_{ij} will be invariant under time reversal if and only if $\tau_{ij}^{(0)}$, $\tau_{ij}^{(o)}$, and $i\tau_{ij}^{(e)}$ are real coefficients. One finds that the even sector is spanned by $\lambda_4, \lambda_5, \lambda_1 - \lambda_6, \lambda_2 - \lambda_7$, and $\lambda_8 - \sqrt{3}\lambda_3$, while the odd sector is spanned by the three spin components $\sqrt{2}J_x = \lambda_1 + \lambda_6$, $\sqrt{2}J_y = \lambda_2 + \lambda_7$, and $2J_z = \lambda_3 + \sqrt{3}\lambda_8$.

As explained above, the hopping matrices T_{ij} in the case of a $SU(N)$ tight-binding model are expressed as $t_{ij}U_{ij}$, where U_{ij} is a unitary matrix with $U_{ij} = \exp(iA_{ij})$. The A_{ij} are $N \times N$ traceless Hermitian matrices reading $A_{ij} = \sum_{n=1}^{N^2-1} \gamma_{ij}^{(n)} \mathcal{T}_n$, with *real* coefficients $\gamma_{ij}^{(n)}$. The matrices A_{ij} represent the gauge field acting on the system and non-Abelian $SU(N)$ models are obtained when the matrices U_{ij} for the different links do not commute, that is, when the matrices A_{ij} do not commute, meaning that a non-Abelian gauge field is acting on the system. The time-reversal operation reads

$$\Theta U_{ij} \Theta^{-1} = e^{\Theta i A_{ij} \Theta^{-1}} = e^{-i \Theta A_{ij} \Theta^{-1}}, \quad (8)$$

such that the tight-binding model is automatically (but not exclusively) invariant under time reversal when the matrices A_{ij} are *odd* under time reversal, i.e., when they have a (real) expansion in the odd sector of the generators \mathcal{T}_n only. (They cannot have a complex expansion on the even sector because of the Hermiticity condition.) This property is the main reason for the difference between $SU(2)$ and $SU(3)$ tight-binding models: for $SU(2)$ the even sector is empty and one can only have odd non-Abelian gauge field matrices A_{ij} and thereby only time-reversal invariant hopping matrices; on the contrary, for $SU(3)$ (and more generally $SU(N)$, with $N \geq 3$), the even sector is not empty such that one can have non-Abelian gauge field matrices A_{ij} resulting in hopping matrices $T_{ij} = t_{ij} \exp(iA_{ij})$ that break time-reversal symmetry and in potentially topologically nontrivial band structures. In Appendix B, we give convenient parametrizations of unitary $U(3)$ matrices which are even or odd under time reversal.

Note, however, that while time-reversal invariance of the system can be directly and safely inferred from gauge fields that reside only in the odd sector, there are cases where time-reversal symmetry is not broken, even though the gauge fields are even under time reversal. For even A_{ij} , time-reversal invariance $e^{\Theta i A_{ij} \Theta^{-1}} = e^{i A_{ij}}$ implies that $\exp(2i A_{ij}) = \mathbb{1}$. For instance, the gauge field $A_{ij} = \frac{\pi}{\sqrt{5}}[(\lambda_1 - \lambda_6) + (\lambda_2 - \lambda_7) + \lambda_4]$ leads to

$$U_{ij} = \exp(iA_{ij}) = \frac{1}{5} \begin{pmatrix} -1 & 2+2i & -4i \\ 2-2i & -3 & -2-2i \\ 4i & -2+2i & -1 \end{pmatrix}, \quad (9)$$

and one has $\Theta U_{ij} \Theta^{-1} = U_{ij}$. In other words, the time-reversal properties of the Hamiltonian are not simply in one-to-one correspondence with those of the gauge field matrices A_{ij} , and ultimately one has to check the property of the hopping matrices T_{ij} themselves.

In conclusion, by choosing suitable A_{ij} having nonvanishing components in the even sector, one can produce hopping matrices T_{ij} that break time-reversal symmetry. This leads to topologically nontrivial spin-1 tight-binding models with a band structure yielding nontrivial Chern numbers [49].

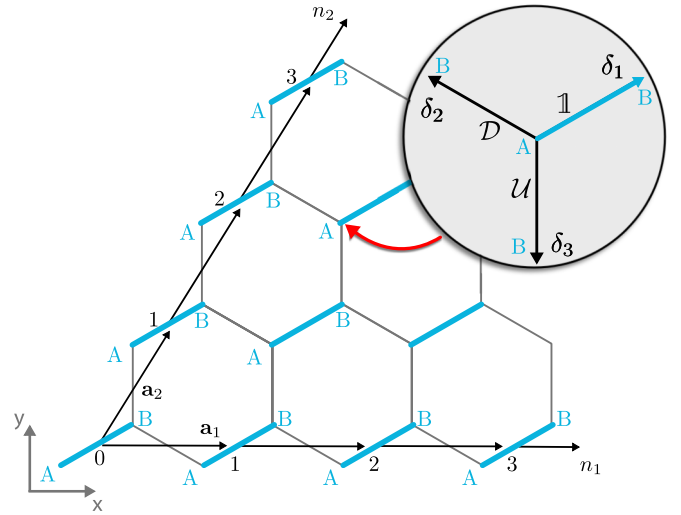


FIG. 1. The non-Abelian $SU(3)$ model on the honeycomb lattice that we investigate. The honeycomb lattice is obtained by repeated translations along Bravais vectors \mathbf{a}_1 and \mathbf{a}_2 of a unit cell containing two inequivalent sites labeled A and B . We assign different spin-orbit couplings on the different A - B links of the honeycomb lattice. The inset shows the nearest-neighbor $SU(3)$ hopping matrices acting on the spin states of the particles: $\mathbb{1}$ along link vectors δ_1 , diagonal hopping phase matrix \mathcal{D} along link vectors δ_2 , and nondiagonal hopping matrix \mathcal{U} along link vectors δ_3 . See main text for their expressions.

B. Non-Abelian $SU(3)$ model on the honeycomb lattice

In the following, we investigate a $SU(3)$ topological insulator consisting of noninteracting spin-1 bosonic particles moving on a honeycomb lattice. Our system and some of the results are similar to those studied in Ref. [49] on the square lattice, where differences are mostly due to the fact that the honeycomb lattice has a two-site unit cell. We are interested in the interplay of the topological properties of the gauge fields with the unique band structure and non-trivial Berry curvature of the honeycomb lattice [55]. The honeycomb lattice is a triangular Bravais lattice obtained by repeated translations $\mathbf{R}(n_1, n_2) = n_1 \mathbf{a}_1 + n_2 \mathbf{a}_2$ (n_1 and n_2 integers) of a unit cell containing two inequivalent sites denoted by A and B , see Fig. 1. Of importance for the following are the link vectors δ_1 , δ_2 , and δ_3 connecting any site A to its three nearest-neighbor sites B . They satisfy $\delta_1 - \delta_2 = \mathbf{a}_1$, $\delta_1 - \delta_3 = \mathbf{a}_2$, and $\delta_1 + \delta_2 + \delta_3 = 0$, see Fig. 1. With our choice of origin in Fig. 1, the positions of all sites A and B in the lattice are labeled by $\mathbf{R}_{n_1, n_2}^A = \mathbf{R}(n_1, n_2) - \delta_1/2$ and $\mathbf{R}_{n_1, n_2}^B = \mathbf{R}(n_1, n_2) + \delta_1/2$. In the following we fix the unit length by setting the lattice constant to unity, i.e., $|\delta_a| = 1$ ($a \in \{1, 2, 3\}$).

We now assign the hopping matrices $T_1 = -t \mathbb{1}$ along links δ_1 , $T_2 = -t \mathcal{D}$ along links δ_2 , and $T_3 = -t \mathcal{U}$ along links δ_3 , with t a (real) hopping rate. The $SU(3)$ matrices $\mathcal{D} = \exp(-\frac{2\pi i}{3} \hat{S}_z)$ and $\mathcal{U} = \exp[-\frac{2\pi i}{3\sqrt{3}}(\lambda_2 - \lambda_5 + \lambda_7)]$ read

$$\mathcal{D} = \begin{pmatrix} j^* & 0 & 0 \\ 0 & 1 & 0 \\ 0 & 0 & j \end{pmatrix} \quad \mathcal{U} = \begin{pmatrix} 0 & 0 & 1 \\ 1 & 0 & 0 \\ 0 & 1 & 0 \end{pmatrix}, \quad (10)$$

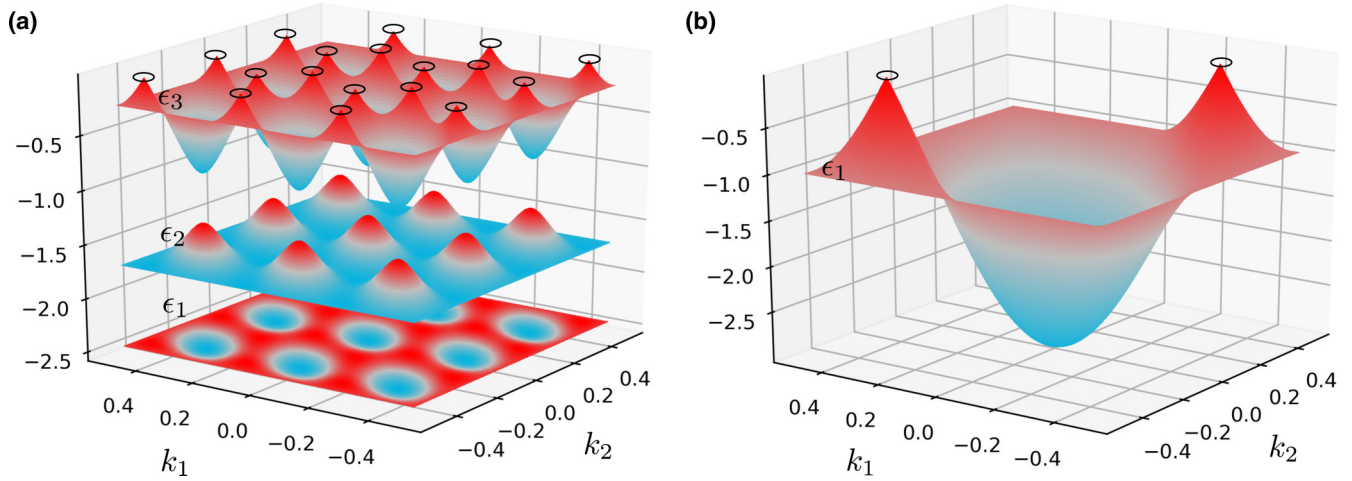


FIG. 2. (a) Bulk spectrum of the Bloch Hamiltonian $\mathcal{H}_{\mathbf{k}}$ given by Eq. (14) in the first Brillouin zone BZ ($|k_{1,2}| \leq 1/2$). Since the full spectrum is symmetric with respect to the zero-energy plane, we only plot the three negative bands $\epsilon_1 \leq \epsilon_2 \leq \epsilon_3 \leq 0$ in units of the tunneling rate t . The small black circles point out the location of Dirac points occurring between the energy bands ϵ_3 and ϵ_4 . (b) Band structure of graphene. The small black circles point out the location of the two Dirac points of graphene. Without the spin-orbit coupling term, our system is equivalent to graphene with threefold degenerate bands (i.e., one copy of the graphene band structure per spin component). The spin-orbit terms couple these three bands, eventually lifting their degeneracy and leading to the spectrum shown in (a). Due to the particular choice of the spin-orbit coupling terms \mathcal{U} and \mathcal{D} , the band structure has the additional translation symmetry: $\epsilon_n(k_1, k_2) = \epsilon_n(k_1 + 1/3, k_2) = \epsilon_n(k_1, k_2 + 1/3)$.

where $j = \exp(2i\pi/3)$. From these expressions, one can check that T_3 is breaking time-reversal symmetry, which gives rise to a band structure with nonvanishing Chern number (see Sec. III below). While spin states are unaffected when particles hop along link vectors δ_1 , they acquire spin-state-dependent phases when particles hop along link vectors δ_2 and they undergo a circular permutation $1 \rightarrow 0 \rightarrow -1 \rightarrow 1$ when particles hop along the link vectors δ_3 . Note that since these matrices fulfill $\mathcal{D}^3 = \mathcal{U}^3 = 1$, a spin state is mapped back to itself after three consecutive hoppings along a given link vector δ_2 or δ_3 . On the contrary, since \mathcal{D} and \mathcal{U} do not commute, the present spin-orbit coupling configuration corresponds to a genuine non-Abelian $SU(3)$ model on the honeycomb lattice: the corresponding gauge fields A_2 and A_3 defined by $T_a = -te^{iA_a}$ ($a = 2, 3$) do not commute and, therefore, the transport of a spin state around a hexagon leads to a nontrivial Wilson loop value $W = 3 \exp(2\pi i/3)$ [69].

III. TOPOLOGICAL PROPERTIES

A. Infinite system–Bulk spectrum

Since the unit cell of the honeycomb lattice hosts two inequivalent sites, it is customary to distinguish the bosonic annihilation and creation operators on A and B sites: $\hat{\mathbf{a}}_{n_1, n_2}^\dagger$ denotes the creation operator on the site \mathbf{R}_{n_1, n_2}^A and $\hat{\mathbf{b}}_{n_1, n_2}^\dagger$ denotes the creation operator on the site \mathbf{R}_{n_1, n_2}^B . Each of them is a spinor of dimension 3 accounting for the three spin states of the spin-1 bosonic particles considered in our model.

Being translation invariant along the Bravais vectors \mathbf{a}_1 and \mathbf{a}_2 , the lattice Hamiltonian is diagonal in momentum space, $\hat{H} = \sum_{\mathbf{k} \in BZ} \hat{H}_{\mathbf{k}}$, where

$$\hat{H}_{\mathbf{k}} = -t (\hat{\mathbf{b}}_{\mathbf{k}}^\dagger M_{\mathbf{k}} \hat{\mathbf{a}}_{\mathbf{k}} + \text{H.c.}), \quad (11)$$

$$M_{\mathbf{k}} = e^{i\mathbf{k} \cdot \delta_1} \mathbb{1} + e^{i\mathbf{k} \cdot \delta_2} \mathcal{D} + e^{i\mathbf{k} \cdot \delta_3} \mathcal{U}. \quad (12)$$

$\hat{\mathbf{a}}_{\mathbf{k}}$ (resp. $\hat{\mathbf{b}}_{\mathbf{k}}$) is the Fourier transform of $\hat{\mathbf{a}}_{n_1, n_2}$ (resp. $\hat{\mathbf{b}}_{n_1, n_2}$); the Bloch wave vector \mathbf{k} belongs to the first Brillouin zone and reads

$$\mathbf{k} = \underbrace{k_1 \mathbf{b}_1}_{\mathbf{k}_1} + \underbrace{k_2 \mathbf{b}_2}_{\mathbf{k}_2}, \quad |k_{1,2}| \leq 1/2, \quad (13)$$

where the honeycomb reciprocal lattice vectors \mathbf{b}_1 and \mathbf{b}_2 are defined by $\mathbf{a}_i \cdot \mathbf{b}_j = 2\pi \delta_{ij}$. Note that with this definition k_1 and k_2 are dimensionless. This parameterization of \mathbf{k} , in turn, allows us to compute a dimensionless Berry curvature, see Eq. (3).

Further defining $\hat{\Phi}_{\mathbf{k}}^\dagger = (\hat{\mathbf{a}}_{\mathbf{k}}^\dagger, \hat{\mathbf{b}}_{\mathbf{k}}^\dagger)$, one can recast this Hamiltonian under the form $\hat{H}_{\mathbf{k}} = \hat{\Phi}_{\mathbf{k}}^\dagger \mathcal{H}_{\mathbf{k}} \hat{\Phi}_{\mathbf{k}}$ where

$$\mathcal{H}_{\mathbf{k}} = -t \begin{pmatrix} 0 & M_{\mathbf{k}}^\dagger \\ M_{\mathbf{k}} & 0 \end{pmatrix}. \quad (14)$$

Diagonalizing the Bloch Hamiltonian $\mathcal{H}_{\mathbf{k}}$ yields six bands $\epsilon_1(\mathbf{k}) \leq \dots \leq \epsilon_6(\mathbf{k})$ where the three (negative) lower bands are mirror images of the three (positive) upper bands with respect to the zero-energy plane, see Fig. 2. This mirror symmetry originates from the bipartite nature of the honeycomb lattice and is also found in the usual band structure of graphene: eigenvalues come in opposite pairs. This is because $P\mathcal{H}_{\mathbf{k}}P = -\mathcal{H}_{\mathbf{k}}$, where P is the diagonal matrix with entries $\mathbb{1}$ and $-\mathbb{1}$ corresponding to the sublattice or chiral symmetry [65,66]. Noting that

$$\mathcal{H}_{\mathbf{k}}^2 = t^2 \begin{pmatrix} N_{\mathbf{k}}^\dagger N_{\mathbf{k}} & 0 \\ 0 & N_{\mathbf{k}} N_{\mathbf{k}}^\dagger \end{pmatrix}, \quad (15)$$

where $N_{\mathbf{k}} = \exp(-i\mathbf{k} \cdot \delta_1) M_{\mathbf{k}}$, it is easy to show that $\epsilon_n^2(\mathbf{k}) = \mu_a^2(\mathbf{k}) t^2$ ($a \in \{1, 2, 3\}$), where $\mu_3^2(\mathbf{k}) \leq \mu_2^2(\mathbf{k}) \leq \mu_1^2(\mathbf{k})$ are the eigenvalues of $N_{\mathbf{k}}^\dagger N_{\mathbf{k}}$ (and also of $N_{\mathbf{k}} N_{\mathbf{k}}^\dagger$). We thus get the band structure $\epsilon_{1,2,3} = -t \mu_{1,2,3}$ and $\epsilon_{4,5,6} = t \mu_{3,2,1}$,

highlighting the mirror symmetry of the bands with respect to the zero-energy plane.

Dirac points are found at points $\mathbf{k} \in BZ$ where two eigenvalues of $N_{\mathbf{k}}^\dagger N_{\mathbf{k}}$ coalesce [70]. Noting that $N_{\mathbf{k}}^\dagger = S N_{-\mathbf{k}} S$, where S is the anti-diagonal matrix with unit entries, we see that $N_{\mathbf{k}}^\dagger N_{\mathbf{k}}$ and $N_{-\mathbf{k}}^\dagger N_{-\mathbf{k}}$, and thus $N_{-\mathbf{k}}^\dagger N_{-\mathbf{k}}$, have the same spectrum. This shows that the Dirac points must come in opposite pairs in the Brillouin zone. In contrast to the graphene band structure which exhibits only one pair of such Dirac points, we get nine pairs of Dirac points here, obtained when $\mu_3(\mathbf{k}) = 0$, that is, between bands $\epsilon_3(\mathbf{k})$ and $\epsilon_4(\mathbf{k})$. The other bands remain fully isolated. Hence, just like graphene, our system is a semimetal. We note that getting nine pairs of Dirac points is not generic but specific to our SU(3) model. It arises from an additional symmetry in our Hamiltonian due to our particular choice of the hopping matrices \mathcal{U} and \mathcal{D} . We point out that this is not because of a smaller effective Brillouin zone since our Hamiltonian, as can be seen from the expression of $M_{\mathbf{k}}$ above, is invariant under Bravais translations only. Instead, one can show that

$$N_{\mathbf{k}+\mathbf{b}_1/3} = \mathcal{U} N_{\mathbf{k}} \mathcal{U}^\dagger, \quad (16)$$

$$N_{\mathbf{k}+\mathbf{b}_2/3} = \mathcal{D}^\dagger N_{\mathbf{k}} \mathcal{D}, \quad (17)$$

meaning that the matrices $N_{\mathbf{k}+\mathbf{b}_i/3}$ ($i = 1, 2$) and $N_{\mathbf{k}}$ are unitarily equivalent. Thus, up to a global gauge transform, the two Hamiltonians $\mathcal{H}_{\mathbf{k}+\mathbf{b}_1/3}$ and $\mathcal{H}_{\mathbf{k}}$ are identical. The same conclusion holds true for Hamiltonians $\mathcal{H}_{\mathbf{k}+\mathbf{b}_2/3}$ and $\mathcal{H}_{\mathbf{k}}$. Going back to the direct lattice, these global gauge transforms amount to a ‘‘rotation’’ of the spin degrees of freedom on each individual lattice site by the same unitary matrix. This shows that the Hamiltonians $\mathcal{H}_{\mathbf{k}+\mathbf{b}_1/3}$, $\mathcal{H}_{\mathbf{k}+\mathbf{b}_2/3}$, and $\mathcal{H}_{\mathbf{k}}$ have the same spectra. We thus infer that $\epsilon_n(\mathbf{k}) = \epsilon_n(\mathbf{k} + \mathbf{b}_1/3) = \epsilon_n(\mathbf{k} + \mathbf{b}_2/3)$ for each energy band.

Note that a mass term such as $\Delta(\hat{n}_A - \hat{n}_B)/2$ breaks the chiral symmetry of the lattice Hamiltonian, since $P\mathcal{H}_{\mathbf{k}}(\Delta)P = -\mathcal{H}_{\mathbf{k}}(-\Delta)$, and lifts the degeneracies between the two middle bands. Indeed, it adds the terms $\Delta/2$ and $-\Delta/2$ on the diagonal entries of $\mathcal{H}_{\mathbf{k}}$, Eq. (14), and the constant term $\Delta^2/4$ on the diagonal entries of $\mathcal{H}_{\mathbf{k}}^2$, leading to $\epsilon_n(\mathbf{k}, \Delta) = \pm t \sqrt{\mu_n^2(\mathbf{k}) + (\Delta/2t)^2}$ and thus to $\epsilon_n(\mathbf{k}, \Delta) = -\epsilon_{7-n}(\mathbf{k}, \Delta)$. Therefore, even though the chiral symmetry is broken, the band structure is still symmetric $E \leftrightarrow -E$. In addition, a closer look at the Bloch wave functions shows that the Berry connections for the band n and $7-n$ have the following structure:

$$\begin{aligned} \mathbf{A}_n(\mathbf{k}, \Delta) &= \mathbf{F}_n(\mathbf{k}) + \frac{\Delta}{\epsilon_n(\mathbf{k}, \Delta)} \mathbf{G}_n(\mathbf{k}), \\ \mathbf{A}_{7-n}(\mathbf{k}, \Delta) &= \mathbf{F}_n(\mathbf{k}) - \frac{\Delta}{\epsilon_n(\mathbf{k}, \Delta)} \mathbf{G}_n(\mathbf{k}). \end{aligned} \quad (18)$$

Although straightforward to derive, the explicit expressions for $\mathbf{F}_n(\mathbf{k})$ and $\mathbf{G}_n(\mathbf{k})$ are quite involved. It is important to note, though, that only $\mathbf{F}_n(\mathbf{k})$ contributes to the Chern number, since the second term \mathbf{G}_n/ϵ_n can be shown to be a periodic function of \mathbf{k} . Alternatively, since $\Delta \oint_{\partial BZ} d\mathbf{k} \cdot \mathbf{G}_n(\mathbf{k})/\epsilon_n(\mathbf{k}, \Delta)$ has to be a multiple of 2π for all values of Δ , the only possibility is that it has a vanishing

value. Note that the structure $[\Delta/\epsilon_n(\mathbf{k}, \Delta)]\mathbf{G}_n(\mathbf{k})$ is very similar to the one found in the usual mass-imbalanced time-reversally symmetric model on a two-site lattice having vanishing Chern numbers [55,71].

This shows that even though the Berry connections and Berry curvatures for the band n and $7-n$ are different for a finite value of Δ , the Chern numbers come in equal pairs $C_n(\Delta) = C_{7-n}(\Delta)$ [72]. Because of this symmetry, the total zero-sum rule of Chern numbers boils down to two separate zero-sum rules $C_1 + C_2 + C_3 = C_4 + C_5 + C_6 = 0$ for all values of Δ . Note that for $\Delta = 0$, one recovers the well-known result that a Hamiltonian invariant under chiral symmetry is topologically trivial *only* if the number of occupied bands is equal to the number of empty bands, i.e., at half-filling. In this case it belongs to the class AIII of Refs. [65,66]. Otherwise, away from half-filling, the system can be topologically nontrivial, belonging to the class A of Refs. [65,66].

We now turn to the numerical computation of the Chern numbers. Strictly speaking, C_n , as given by Eq. (2), is only well-defined for an isolated band. Since the two middle bands ϵ_3 and ϵ_4 are touching, we add a small mass term $\Delta = 0.1t$ such that the six bands are fully isolated. Following [73], this allows one to safely compute C_n for each band and quantify the topology of the band structure. Alternatively, one could also adjust the grid used to compute the Chern number in [73] as to avoid the Dirac points. The latter approach has been checked by calculating the combined two-band Chern number C_{34} for these two middle bands [73]. According to the sublattice symmetry, it should be twice the individual band Chern numbers, i.e., $C_{34} = 2C_3 = 2C_4$. Both the finite mass method and the adjusted grid method confirm this result. For our SU(3) model, we find $C_1 = 3$, $C_2 = -6$, and $C_3 = 3$ [74]. These nonzero values signal nontrivial topological properties of the bulk band structure.

B. Finite system–Edge states

As is well known, a lattice Hamiltonian having a band structure with nonvanishing Chern numbers exhibits edge states in a strip geometry [64]. We consider such a finite lattice strip for our SU(3) model and compute the spectrum for open boundary conditions in the \mathbf{a}_1 direction ($0 \leq n_1 \leq N$) and periodic boundary conditions in the \mathbf{a}_2 direction (unrestricted n_2). The lattice strip we consider has left and right zigzag boundaries. Since the Hamiltonian is still invariant under lattice translations along \mathbf{a}_2 , the Bloch wave vector along \mathbf{b}_2 remains a good quantum number. Therefore, we introduce the Fourier transform operators $\hat{\mathbf{a}}_{n_1, k_2}$ and $\hat{\mathbf{b}}_{n_1, k_2}$ along \mathbf{a}_2 . The Hamiltonian, for a given Bloch wave vector k_2 , now reads

$$\begin{aligned} \hat{H}_{k_2} &= -t \sum_{n_1=0}^N \hat{\mathbf{b}}_{n_1, k_2}^\dagger (e^{ik_2 \cdot \delta_1} \mathbb{1} + e^{ik_2 \cdot \delta_3} \mathcal{U}) \hat{\mathbf{a}}_{n_1, k_2} \\ &\quad - t \sum_{n_1=1}^N \hat{\mathbf{b}}_{n_1-1, k_2}^\dagger e^{ik_2 \cdot \delta_2} \mathcal{D} \hat{\mathbf{a}}_{n_1, k_2} + \text{H.c.}, \end{aligned} \quad (19)$$

with $|k_2| \leq 1/2$. By diagonalizing \hat{H}_{k_2} , we obtain the band spectrum shown in Fig. 3. This spectrum has to be compared to the bulk spectrum, shown in Fig. 4, that has been obtained for the same number of cells N along \mathbf{a}_1 but with periodic

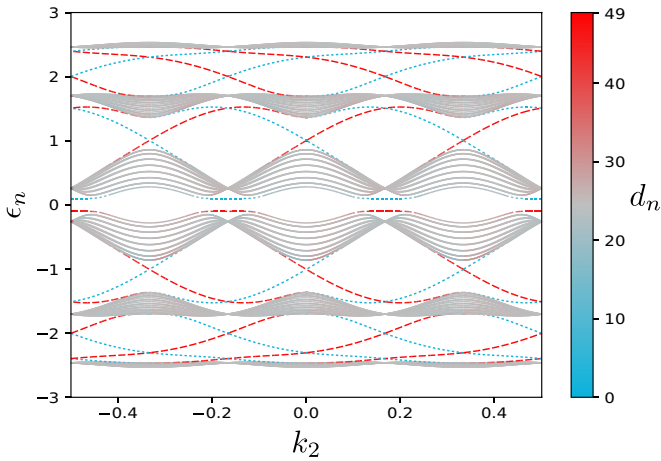


FIG. 3. Spectrum ϵ_n in units of the tunneling rate t , obtained by diagonalizing the Hamiltonian Eq. (19) describing a finite lattice strip with $N = 25$ cells, i.e., 50 sites, along \mathbf{a}_1 (open boundary conditions) and periodic boundary conditions along \mathbf{a}_2 . The mass term is $\Delta = 0.1$. Compared to Fig. 4, we see the appearance of topological edge states in the gaps between the bulk bands with different Chern numbers. No such edge states develop between bulk bands ϵ_3 and ϵ_4 since they have equal Chern numbers. The color scale on the right side shows the average position d_n of the eigenstates along \mathbf{a}_1 . The dotted blue lines (resp. dashed red lines) correspond therefore to edge states localized on the left (resp. right) side of the strip. As one can see, the topological states connecting two bands live on either side of the strip while the other bulklike states spread over the whole strip. Comparing this band structure to a similar system on the square lattice [49], we find that the lower three bands in this figure and the edge states between them are largely the same as on the square lattice. This is confirmed by the same Chern numbers of both cases. Due to the two-site unit cell of the honeycomb lattice, this band structure is mirrored around $\epsilon = 0$, resulting in six bands in our case. Where the two middle bands are touching, artefacts of the original honeycomb lattice remain in the form of Dirac cones (see also Figs. 2 and 4).

boundary conditions. As expected from our analysis of the bulk spectrum [60–64], we indeed find additional states in the gaps between bands with different Chern numbers, that is, between the first and second bands, between the second and third bands, and, by symmetry, between the fourth and fifth bands and between the fifth and sixth bands. The states between the third and the fourth band, on the other hand, are topologically trivial edge states that are characteristic to the single-particle band structure of the honeycomb lattice [75]. Their spatial behavior depends on the shape of the edge of the honeycomb strip and they become flat in the limit of the semi-infinite plane. Their wave functions are not localized on a given edge but are generally symmetric around the middle of the lattice strip, with more weight on the edges than in the bulk. Due to this symmetry, these edge states are trivial in the sense that they lack the chirality of the topological edge states. This is consistent with the fact that the third and the fourth band have equal Chern numbers.

We define the position x_i ($x_i = 1, \dots, 2N$) of the sites along a given horizontal zigzag chain crossing the lattice strip from left to right and we denote by $P_n(x_i, k_2)$ the spatial

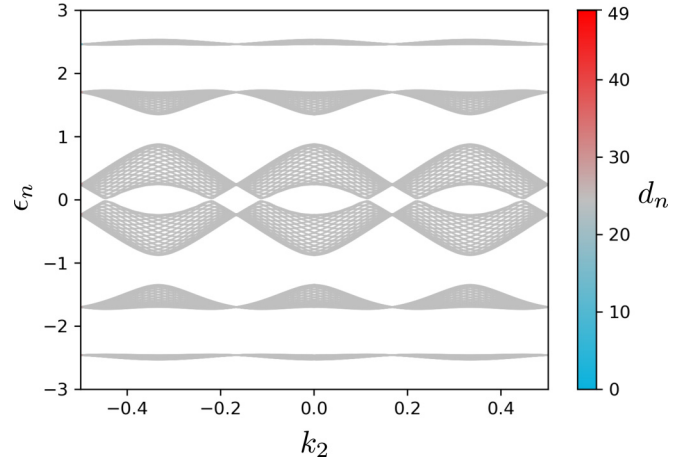


FIG. 4. Bulk spectrum, in units of the tunneling rate t , obtained by diagonalization of the Hamiltonian Eq. (14) with periodic boundary conditions both along \mathbf{a}_1 and \mathbf{a}_2 . The number of cells along \mathbf{a}_1 is $N = 25$ and the mass term is $\Delta = 0$. The color scale shows the average position d_n of the eigenstates along \mathbf{a}_1 . All eigenstates are spread out over the lattice, and their average position d_n is the middle of the lattice.

distribution of the eigenstate with eigenvalue $\epsilon_n(k_2)$ along this chain. The color scale of Fig. 3 shows the average position

$$d_n = \sum_i x_i P_n(x_i, k_2) \quad (20)$$

of the eigenstate in the strip. We see that states chosen within the bulklike bands spread uniformly over the whole lattice strip, and d_n lies at the center of the lattice strip. On the contrary, states connecting bulklike bands with different Chern numbers are either strongly localized on the left boundary (black) or on the right boundary (green) of the lattice: these are the celebrated edge states. We also see that, in our system, edge states within a given gap are localized on one side of the strip when their group velocity is positive and on the other side of the strip when their group velocity is negative. This one-to-one correspondence between the sign of the slope of the energy dispersion relation of an edge state and its spatial localization changes from one gap to the other. This feature, particular to our system, emphasizes the chiral character expected for particle transport at the boundaries. Interestingly, one can recover the values of the Chern numbers of our bulk system from the bulk-edge correspondence [60–62]. Within a given gap, one counts the number of edge states N_+ and N_- with positive and negative group velocities that give rise to a localization on the right side of the strip. The difference ($N_+ - N_-$) is then equal to the sum of the Chern numbers of all the bands below the gap considered. This recipe allows one to reconstruct all Chern numbers with their sign. It is easy to check that we recover the values computed in the preceding paragraph. For instance, the absence of edge states linking the third and the fourth bands ($N_+ = N_- = 0$) is in agreement with the fact that the sum of the Chern numbers of the three lowest bands vanishes, $N_+ - N_- = C_1 + C_2 + C_3 = 0$.

The probability distribution $P_n(x_i, k_2) \propto e^{\gamma x_i}$ of an edge state decays exponentially with x_i when it is localized at $x_i = 0$ ($\gamma < 0$) and grows exponentially with x_i when it is

localized at $x_i = 2N$ ($\gamma > 0$). The (positive or negative) value of the characteristic scale $1/\gamma$ depends both on the edge state considered and on the Bloch wave vector k_2 . This is emphasized in Fig. 5(b), where we plot γ as a function of k_2 for the edge states with the dispersion relation highlighted in Fig. 5(a). As one can see, the state is localized on the left side of the strip ($x_i = 0$) as long as its group velocity is negative. For values of k_2 roughly in the range 0.3–0.4, the state dives into the bulk band and becomes delocalized. The decay coefficient γ then vanishes. For larger k_2 values, the group velocity becomes positive and the state is now localized on the right side of the strip ($x_i = 2N$). Finally, Fig. 5(c) shows the probability distribution P_n for the different edge states shown in Fig. 5(a) for a given value of $k_2 \simeq 0.458$. Here again, one can see the correlation observed in our system between the sign of the group velocity and the localization center of the edge state.

IV. TOPOLOGICAL TRANSITIONS

The Chern number of a given isolated band is an invariant integer-valued topological quantity. Its value can only change when the band comes in contact with another one. A closing gap can be achieved by changing parameters in the Hamiltonian, for example, the strength of the spin-orbit coupling. In general, the hopping matrices along links δ_a can be written as $T_a = -t \exp(iA_a)$ ($a \in \{1, 2, 3\}$). The traceless Hermitian gauge field can be written as $A_a = \alpha_a \cdot \lambda$, where α_a is a real eight-component vector and λ is the eight-component vector made of the Gell-Mann matrices. We have first monitored the band structure, gaps, and Chern numbers by considering various configurations of the three vectors α_a . However, for all configurations that we tested, we could only recover the set of Chern numbers (3, -6, 3) already found in Sec. III for the three negative bands, or the opposite set (-3, 6, -3). The same result was obtained by allowing for imbalanced tunneling amplitudes, that is, $T_a = -t_a \exp(iA_a)$, and by varying t_a .

More saliently, we found other topological transitions giving rise to different sets of Chern numbers by adding a spin-dependent chemical potential term $-\sum_{\sigma} (\mu_A^{\sigma} \hat{n}_A^{\sigma} + \mu_B^{\sigma} \hat{n}_B^{\sigma})$ with spin $\sigma \in \{-1, 0, 1\}$ to the Hamiltonian. The chemical potential for A sites reads $\mu_A^{\sigma} = -\Delta/2 + \sigma \delta \mu_A$ and $\mu_B^{\sigma} = \Delta/2 + \sigma \delta \mu_B$ for B sites. Note that Δ is the usual (spin-independent) mass term (see Sec. III). All in all, we found that the two following spin-dependent chemical potential configurations:

1. $\delta \mu_B = -\delta \mu_A = \Delta_S/2$ (spin-dependent mass imbalance)

2. $\delta \mu_B = \delta \mu_A$ (spin-dependent local potential)

with an additional spin-orbit coupling along δ_1 giving rise to a larger variety of Chern numbers. We point out that without this additional spin-orbit coupling, one can still find Chern numbers differing from $\pm(3, -6, 3)$, but only for some particular values of the spin-orbit couplings along δ_2 and δ_3 . The additional spin-orbit coupling modifies the value of the Wilson loop around an elementary plaquette: $W \approx 0.38 - i \times 0.67$. Note that in this case $|W| < 3$, emphasizing that one is in a non-Abelian regime.

As an example, we consider a system with spin-dependent mass imbalance ($\Delta_S \neq 0$) and non-Abelian hopping matrices

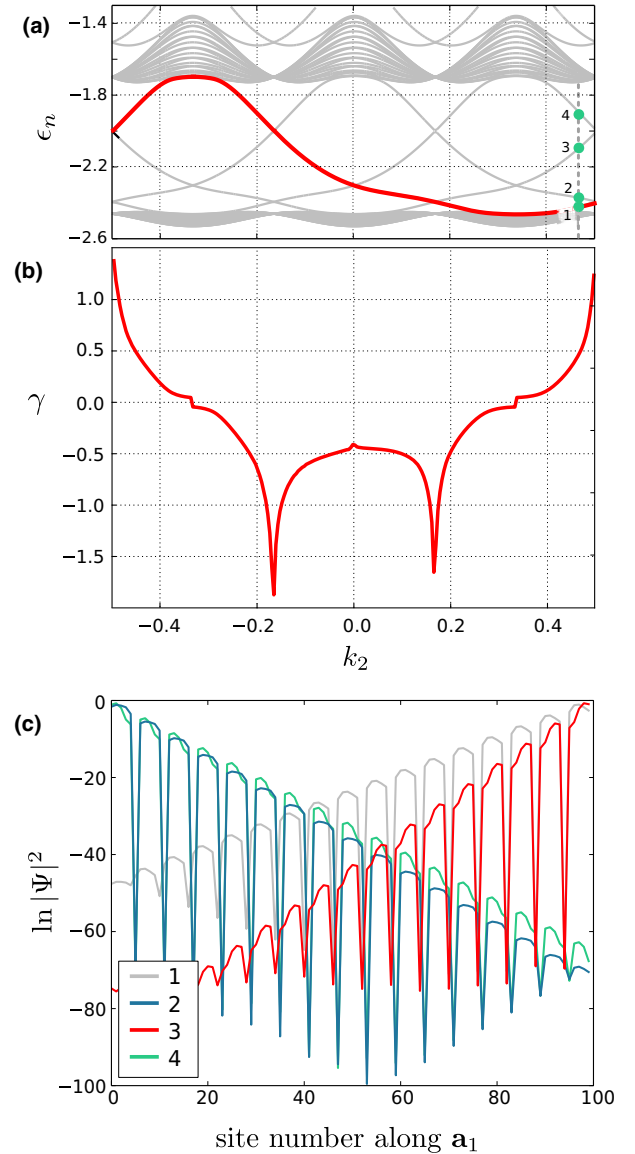


FIG. 5. Localization properties of edge states. (a) Zoom of the band structure shown in Fig. 3 in terms of the tunneling rate t . We consider the edge states associated to the eigenvalues highlighted in red (thick line) and the edge states 1, 2, 3, and 4 (green dots) obtained at the particular value $k_2 \simeq 0.458$. Edge states 1 and 3 have positive group velocities, while states 2 and 4 have negative group velocities. The probability distribution $P_n(x_i, k_2)$ of these states behave like $\exp(\gamma x_i)$ with $\gamma \geq 0$ when the state is localized on the right side of the lattice strip and $\gamma \leq 0$ when it is localized on its left side. (b) Plot of $\gamma(k_2)$ for the edge states with energy dispersion relation highlighted in red in panel (a). As one can see, states with negative group velocities are localized at $x_i = 0$ and $\gamma < 0$. For values of k_2 roughly between 0.3 and 0.4, the states dive into the bulk band, become delocalized, and γ vanishes. For larger k_2 values, the group velocity becomes positive, and the edge states are now localized at $x_i = 2N$ and $\gamma > 0$. (c) Plot of $\ln P_n$ as a function of x_i along a horizontal zigzag chain crossing the lattice strip for the edge states 1 (light colored line, right side), 2 (dark colored line, left side), 3 (dark colored line, right side), and 4 (light colored line, left side) indicated in panel (a). Their localization is correlated with the sign of their group velocity. We see that the closer the state to the bulklike band, the smaller γ .

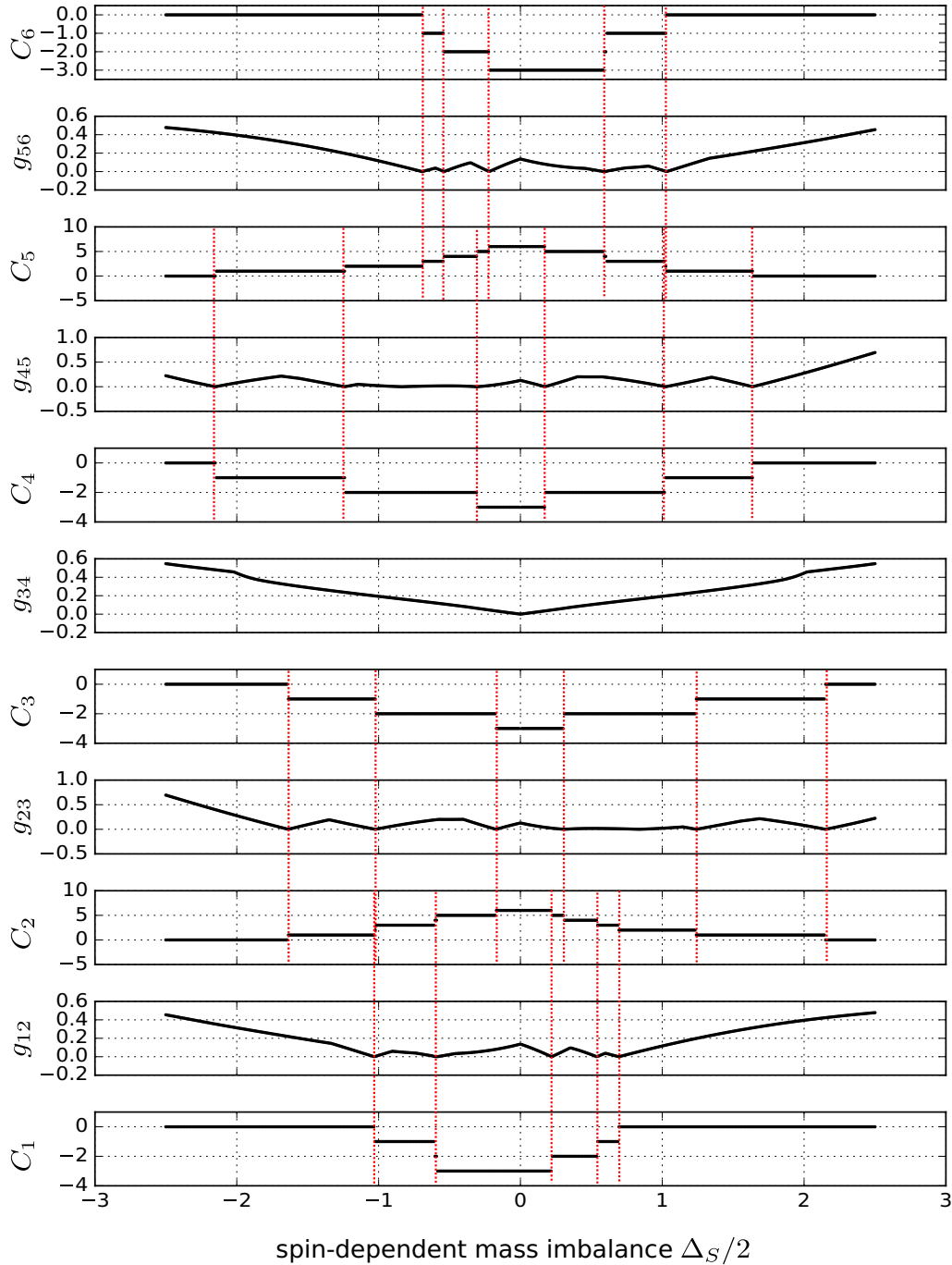


FIG. 6. Chern numbers C_n and band gaps $g_{n+1,n} = \text{Min}[\epsilon_{n+1}(\mathbf{k}, \Delta_S) - \epsilon_n(\mathbf{k}, \Delta_S)]$ (in units of the tunneling rate t) as functions of the spin-dependent mass imbalance $\Delta_S/2$ (in units of the tunneling rate t). Many topological transitions are observed, resulting in various integer changes of the Chern number values, which are no longer restricted to $\pm(3, -6, 3)$ (see text). The red-dotted vertical lines are guides to the eye emphasizing that a change in Chern numbers is always associated with a vanishing gap between two bands. Gap g_{23} between 0.3 and 1.3 (and g_{45} between -0.3 and -1.3) is generally open although amplitudes are small. It closes at the points of transitions between different sets of Chern numbers, but also at $\Delta_S/2 \approx 0.84t$. In this case, even though the gap closes and the Chern numbers become ill defined as in a true topological transition, the Chern numbers remain the same on either side of that critical point. Since $H(\Delta_S)$ maps to $-H(-\Delta_S)$, we have $C_{7-n}(\Delta_S) = C_n(-\Delta_S)$ (see text). For $\Delta_S = 0$, one recovers the expected set of Chern numbers $(-3, 6, -3)$.

$T_1 = -t \mathcal{V} = -t \exp(iA_1)$, where $A_1 = \frac{2\pi}{3\sqrt{3}}(\lambda_1 + \lambda_4 + \lambda_6)$, $T_2 = -t \mathcal{D}$, and $T_3 = -t \mathcal{U}$. For the sake of simplicity, we also choose $\Delta = 0$. Figure 6 shows the six Chern numbers C_n and the different band gaps that are obtained as a function of Δ_S .

As one can see, we get new sets of Chern numbers now and not just $\pm(3, -6, 3)$, see Table I. The vertical lines in Fig. 6 are guides to the eye that mark a gap closing between two adjacent bands. We see that the different gaps do not close

TABLE I. The different sets of Chern numbers obtained for the three upper bands for increasing values of Δ_S (see Fig. 6). At $\Delta_S = 0$, one recovers the expected set of Chern numbers $(-3, 6, -3)$. The values for the three lowest bands are obtained from the symmetry relation $C_{7-n}(\Delta_S) = C_n(-\Delta_S)$. They satisfy the zero-sum rule $C_6 + C_5 + C_4 = 0$ for each value of Δ_S (see text).

C_6	0	-1	-2	-3	-2	-1	0
C_5	0	1	2	3	4	5	6
C_4	0	-1	-2	-3	-2	-1	0

at the same time. This emphasizes that it is only the pair of Chern numbers C_{n+1} and C_n of the bands involved in the gap closing $g_{n+1,n} = 0$ that can change. One has

$$(C_{n+1} + C_n)_{\text{after}} = (C_{n+1} + C_n)_{\text{before}}, \quad (21)$$

with the other Chern numbers remaining unaffected.

This process can be witnessed in Fig. 7, where we plot the two topmost bands of the spectrum and the edge states in between over a topological transition achieved by varying $\Delta_S/2$. For smaller $|\Delta_S/2|$, we see that the bands are gapped and the edge states are connecting neighboring bands. For larger $|\Delta_S/2|$ the edge states coincide with the two neighboring bulk bands at their band-touching point. This is the topological transition point. For even larger $|\Delta_S/2|$ the bulk bands open up again and the edge states move up in sync with the upper band, no longer connecting neighboring bands. Now there is one pair of edge states less, that formerly connected two bands of the spectrum, and we know from the bulk-edge correspondence that this process must have changed the Chern number.

Note that this is a purely local process that is responsible for the change of a global quantity—the Chern number. This is shown in Fig. 8, where we plot the exponent γ that describes the decay of the localized edge wave functions for the two edge states at $k_2 = 0.16$ in Fig. 7. This point in the Brillouin zone is close to, but not exactly at the transition point. The

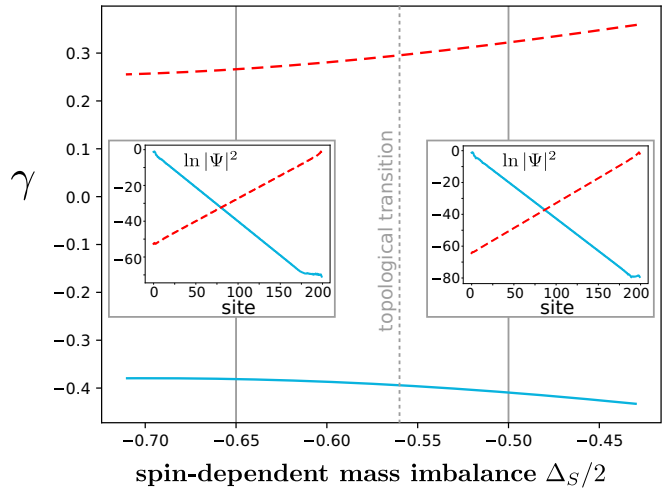


FIG. 8. Edge-state behavior close to the topological transition point ($k_2 = 0.16$). As shown in Fig. 5, the probability distribution $P_n(x_i, k_2)$ of these states behaves like $\exp(\gamma x_i)$, with $\gamma \geq 0$ when the state is localized on the right side of the lattice strip and $\gamma \leq 0$ when it is localized on its left side. Considering the two edge states shown in the left half of the plots in Fig. 7, we plot γ over the spin-dependent mass imbalance $\Delta_S/2$ in units of the tunneling rate t over the topological transition shown in Fig. 7. The red (dashed) line corresponds to the edge state localized on the right side ($d_n \approx 199$) of the lattice (Fig. 7), and the blue (solid) line corresponds to the edge state localized on the left side ($d_n \approx 0$) of the lattice. We notice that away from the transition point the edge state wave function has a smooth behavior during a topological transition. The insets show the corresponding wave functions for $\Delta_S/2 = -0.65t$ and $\Delta_S/2 = -0.5t$. The wave functions of the same state (red and blue, respectively) have qualitatively the same shape with only slight variations in the exponent on both sides of the topological transition.

blue line corresponds to the edge state in Fig. 7 that is localized on the left $d_n \approx 0$ side of the lattice strip (blue line). The red line corresponds to the edge state localized on the

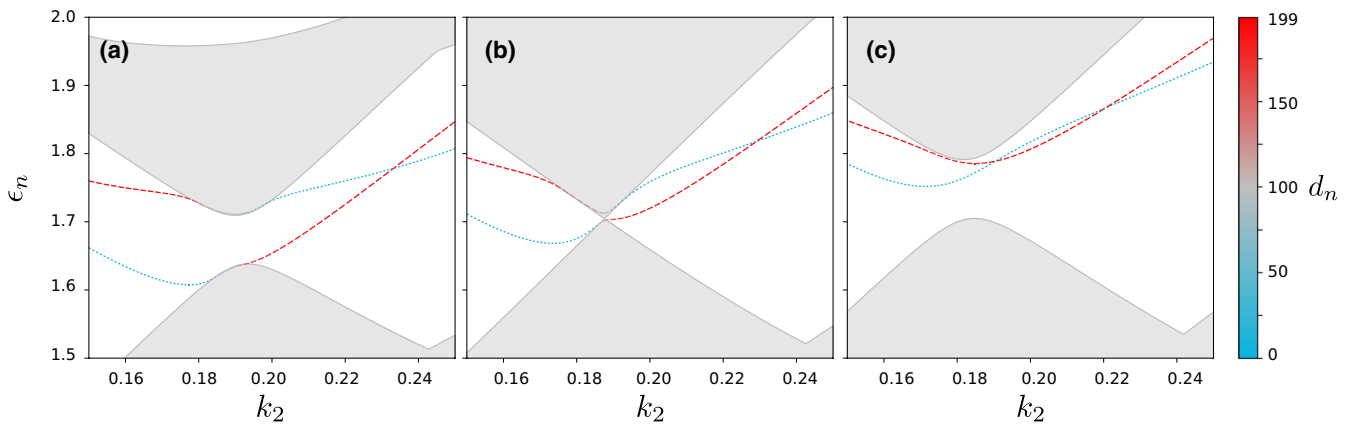


FIG. 7. Spectrum ϵ_n in units of the tunneling rate t during a topological transition. We plot the envelopes of the two uppermost bands (5th and 6th) and the edge states in between. d_n denotes the average localization of the states [Eq. (20)], where the edge states in the gap are localized on either side of the lattice while the bulk states in the bands are spread out over the whole lattice. The dotted blue lines (resp. dashed red lines) correspond therefore to edge states localized on the left (resp. right) side of the strip. During a topological transition, crossing edge states split up at the same point where the bands are touching. The spectra are plotted for $N = 100$ cells and mass terms $\Delta/2 = 0.1t$. (a) $\Delta_S/2 = -0.43t$, (b) $\Delta_S/2 = -0.56t$, (c) $\Delta_S/2 = -0.71t$.

right $d_n \approx 199$ side of the lattice strip (red line) accordingly. The edge-state wave functions at $k_2 = 0.16$ change smoothly with $\Delta_S/2$, even though a topological transition takes place in its immediate vicinity.

Although a topological transition takes place in the close vicinity of the quasimomentum k_2 that we choose to plot the edge-state wave functions for, the edge-state wave functions change smoothly over the interval of the spin-dependent mass imbalance $\Delta_S/2$ triggering the topological transition.

Like in Sec. III, finite values of Δ or Δ_S break the chiral symmetry, but one has $P\mathcal{H}_{\mathbf{k}}(\Delta, \Delta_S)P = -\mathcal{H}_{\mathbf{k}}(-\Delta, -\Delta_S)$. As a consequence, changing the sign of all the mass imbalances amounts to flipping the sign of the eigenvalues of the Hamiltonian, $\epsilon_n(\mathbf{k}, -\Delta, -\Delta_S) = -\epsilon_{7-n}(\mathbf{k}, \Delta, \Delta_S)$, and thereby one can derive that $C_{7-n}(\Delta, \Delta_S) = C_n(-\Delta, -\Delta_S)$. This symmetry in the Chern numbers can be readily checked in Fig. 6, obtained for $\Delta = 0$. One also confirms that gaps have the same symmetry, $g_{n+1,n}(\Delta_S) = g_{7-n,6-n}(-\Delta_S)$, from which one concludes that g_{43} is symmetric in Δ_S . We also note that the gap g_{43} only closes at $\Delta_S = 0$ but that this degeneracy does not modify C_3 and C_4 . As a consequence, the change in Chern numbers after a gap closing can only occur within the subset (C_1, C_2, C_3) or within (C_4, C_5, C_6) . The Chern numbers thus satisfy again the separate zero-sum rules $C_1 + C_2 + C_3 = C_4 + C_5 + C_6 = 0$. Finally, all bands eventually reach a vanishing Chern number for large enough values of $|\Delta_S|$, even though the Berry curvatures neither vanish nor display any particular symmetry. Figure 9 shows a plot of the Berry curvature of the second band $\epsilon_2(\mathbf{k}, \Delta_S)$ in the Brillouin zone obtained for $\Delta_S = -2.6t$ where $C_2 = 1$ (top plot) and for $\Delta_S = -4t$ where $C_2 = 0$ (bottom plot). In both cases, the Berry curvatures exhibit qualitatively similar structures.

As explained above, such a rich variety of Chern numbers and topological transitions have been obtained by imposing spin-dependent chemical potentials on sites A and B and different spin-orbit couplings along the three links, keeping intact, at the same time, the underlying triangular Bravais symmetry of the honeycomb lattice. We have studied the same situation on the square lattice (not shown here) but were not able, in general, to find such a rich variety of Chern numbers and topological transitions. More precisely, for the honeycomb lattice, a generic configuration, i.e., chosen at random, of different spin-orbit couplings along the three links together with spin-dependent chemical potential almost always leads to Chern numbers differing from $\pm(-3, 6, -3)$. The situation is the opposite for the square lattice: for random spin-orbit couplings and spin-dependent chemical potentials, a lot of configurations still correspond to Chern numbers equal to $\pm(3, -6, 3)$. From that point of view, the $SU(3)$ model on the honeycomb lattice exhibits a band structure with richer topological properties. Another argument is that tight-binding models have a finite number of bands and the Chern numbers sum up to 0. Since the square lattice has three bands, leading to $C_1 + C_2 + C_3 = 0$, and the honeycomb lattice has six, leading to $C_1 + C_2 + C_3 + C_4 + C_5 + C_6 = 0$, the set of all possible Chern numbers is obviously larger for the honeycomb lattice than for the square lattice.

A similarly rich variety of topological transitions and Chern numbers is obtained by allowing for complex α_a in the gauge fields $A_a = \alpha_a \cdot \lambda$. However, this situation, even if

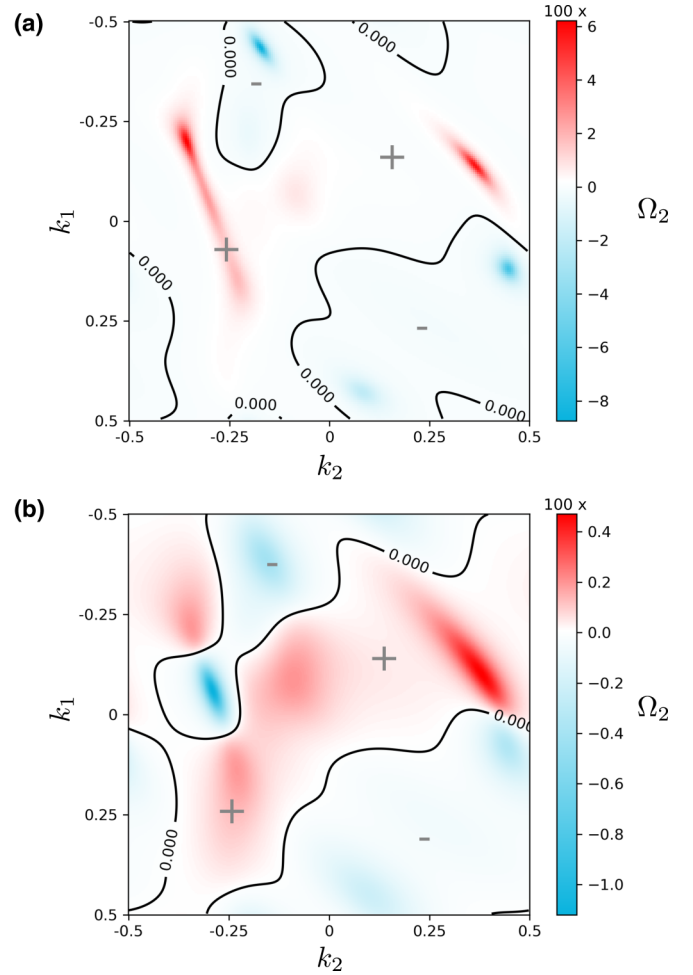


FIG. 9. Plot of Berry curvature $\Omega_2(\mathbf{k}, \Delta_S)$ and the level curve $\Omega_2 = 0$ for the second band $\epsilon_2(\mathbf{k}, \Delta_S)$, see Fig. 6. Positive regions are marked by “+” signs and negative regions by “-” signs. Top plot: $\Delta_S = -2.6t$ ($C_2 = 1$). Bottom plot: $\Delta_S = -4t$ ($C_2 = 0$). Both Berry curvatures exhibit qualitatively similar structures. In particular, there is no obvious particular pattern or symmetry explaining why C_2 vanishes when $\Delta_S = -4t$.

experimentally feasible, does not correspond to a pure $SU(3)$ gauge potential anymore.

We emphasize that the bulk bands remain well isolated for a large variety of gauge fields A_a and for many values of the spin-dependent mass imbalance Δ_S . However, even though the bands do not touch at any point in the Brillouin zone, they can still overlap on the energy axis, which means that there is no *charge* gap separating them. This situation is depicted in Fig. 10 for $\Delta = \Delta_S = 0$, $T_1 = -t\mathcal{U}$, $T_2 = -t\mathcal{D}$, and $T_3 = -t\mathcal{V}$. But, since the Chern numbers are still well defined, topological edge states linking the different bands still appear in the strip lattice configuration. On the other hand, the absence of charge gaps prevents the system from behaving like a Chern insulator and no Hall plateaus are expected in transverse conductance measurements.

V. CONCLUSION

We have studied time-reversal symmetry and topological properties of a noninteracting tight-binding model on the

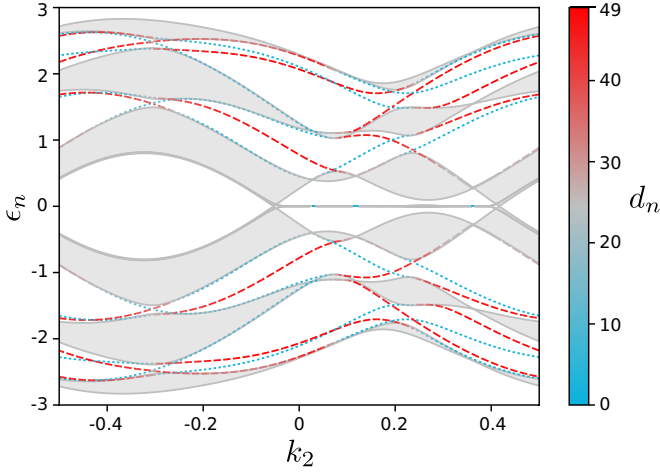


FIG. 10. Band structure ϵ_n (in units of the tunneling rate t) for the strip lattice configuration when $\Delta = \Delta_S = 0$, $T_1 = -tU$, $T_2 = -tD$, and $T_3 = -tV$ (see text). Even though the bulklike bands (their envelopes plotted in gray here) are well isolated and thus never touch anywhere in the Brillouin zone, there is no finite charge gap separating them anymore. The Chern numbers being well defined, edge states are still present and link the different bands. The color scale on the right side shows the average position d_n of the eigenstates along \mathbf{a}_1 . The dotted blue lines (resp. dashed red lines) correspond therefore to edge states localized on the left (resp. right) side of the strip. Because of the absence of a charge gap, the system is not a Chern insulator.

honeycomb lattice with SU(3) spin-orbit couplings. We have emphasized that, in marked contrast with lattice SU(2) models which are always topologically trivial, these SU(3) models can break time-reversal invariance. As a consequence, their bulk band structure becomes topologically nontrivial: bulk bands have nonzero Chern numbers and chiral edge states develop in a lattice strip configuration with open boundary conditions. We have also shown that SU(3) models on the honeycomb lattice allow for a larger variety of sets of Chern numbers than on the square lattice [49], where Chern numbers are mostly multiples of 3. This is due to the topology of the honeycomb lattice, which has two sites per cell and three nonequivalent links, allowing for three different spin-orbit couplings, whereas the square lattice only allows for two spin-orbit couplings on two different links.

A natural extension of the present work is to include interactions in our model and understand their impact on the topological properties of our system. In particular, one expects

the emergence of nontrivial spin textures in the ground state to break the translation symmetry of the lattice [32,33,50,52], and because SU(3) is a larger gauge group than SU(2), we expect a much larger variety of topological properties for these spin textures [19,54]. In addition, the topological properties of the band structure of the noninteracting system are expected to translate into topological properties of the band structure of the low-energy excitations: magnons in Mott phases and Bogoliubov modes in the superfluid phases [55].

ACKNOWLEDGMENTS

The Centre for Quantum Technologies is a Research Centre of Excellence funded by the Ministry of Education and National Research Foundation of Singapore.

APPENDIX A: GELL-MANN MATRICES

The generators of the SU(3) group are $g_a = \lambda_a/2$, where the λ_a are the Gell-Mann matrices:

$$\lambda_1 = \begin{pmatrix} 0 & 1 & 0 \\ 1 & 0 & 0 \\ 0 & 0 & 0 \end{pmatrix} \quad \lambda_2 = \begin{pmatrix} 0 & -i & 0 \\ i & 0 & 0 \\ 0 & 0 & 0 \end{pmatrix} \quad (\text{A1})$$

$$\lambda_3 = \begin{pmatrix} 1 & 0 & 0 \\ 0 & -1 & 0 \\ 0 & 0 & 0 \end{pmatrix} \quad \lambda_4 = \begin{pmatrix} 0 & 0 & 1 \\ 0 & 0 & 0 \\ 1 & 0 & 0 \end{pmatrix} \quad (\text{A2})$$

$$\lambda_5 = \begin{pmatrix} 0 & 0 & -i \\ 0 & 0 & 0 \\ i & 0 & 0 \end{pmatrix} \quad \lambda_6 = \begin{pmatrix} 0 & 0 & 0 \\ 0 & 0 & 1 \\ 0 & 1 & 0 \end{pmatrix} \quad (\text{A3})$$

$$\lambda_7 = \begin{pmatrix} 0 & 0 & 0 \\ 0 & 0 & -i \\ 0 & i & 0 \end{pmatrix} \quad \lambda_8 = \frac{1}{\sqrt{3}} \begin{pmatrix} 1 & 0 & 0 \\ 0 & 1 & 0 \\ 0 & 0 & -2 \end{pmatrix}. \quad (\text{A4})$$

They satisfy $\text{Tr}(\lambda_a \lambda_b) = 2\delta_{ab}$. One can easily check that

$$\begin{aligned} \Theta \lambda_1 \Theta^{-1} &= -\lambda_6 & \Theta \lambda_2 \Theta^{-1} &= -\lambda_7 & \Theta \lambda_4 \Theta^{-1} &= \lambda_4 \\ \Theta \lambda_5 \Theta^{-1} &= \lambda_5 & \Theta \lambda_6 \Theta^{-1} &= -\lambda_1 & \Theta \lambda_7 \Theta^{-1} &= -\lambda_2 \\ \Theta \lambda_3 \Theta^{-1} &= \frac{\lambda_3 - \sqrt{3}\lambda_8}{2} & \Theta \lambda_8 \Theta^{-1} &= -\frac{\lambda_8 + \sqrt{3}\lambda_3}{2}. \end{aligned} \quad (\text{A5})$$

APPENDIX B: TIME-REVERSAL AND UNITARY MATRICES

Time-reversal symmetric unitary matrices $U \in U(3)$ have a parametrization $U_{\text{even}} = \pm \frac{1}{1+\cos^2 \phi} M_{\text{even}}$ with

$$M_{\text{even}} = \begin{pmatrix} 2 \cos^2 \phi e^{i\chi_a} & 2 \sin \phi \cos \phi e^{\frac{i}{2}(\chi_a + \chi_b)} e^{i\pi n} & \sin^2 \phi e^{i\chi_b} \\ -2 \sin \phi \cos \phi e^{\frac{i}{2}(\chi_a - \chi_b)} e^{i\pi n} & 2 - 3 \sin^2 \phi & 2 \sin \phi \cos \phi e^{-\frac{i}{2}(\chi_a - \chi_b)} e^{-i\pi n} \\ \sin^2 \phi e^{-i\chi_b} & -2 \sin \phi \cos \phi e^{-\frac{i}{2}(\chi_a + \chi_b)} e^{-i\pi n} & 2 \cos^2 \phi e^{-i\chi_a} \end{pmatrix}, \quad (\text{B1})$$

where the angles ϕ , χ_a , and χ_b are arbitrary real parameters and n is an arbitrary integer. Since $\text{Det}(\Theta U_{\text{even}} \Theta^{-1}) = \text{Det}(U_{\text{even}}^*) = (\text{Det } U_{\text{even}})^* = \text{Det } U_{\text{even}}$, we conclude that $\text{Det } U_{\text{even}}$ is real and U_{even} is unimodular: $\text{Det } U_{\text{even}} = \pm 1$. This can be directly checked from the matrix expression given above. This result is in fact general: any unitary $N \times N$ matrix which is even under time reversal is unimodular.

If U is odd under time reversal, a convenient parametrization is $U_{\text{odd}} = \pm \frac{1}{1+\cos^2\phi} M_{\text{odd}}$ with

$$M_{\text{odd}} = \begin{pmatrix} 2\cos^2\phi e^{i\chi_a} & 2\sin\phi\cos\phi e^{\frac{i}{2}(\chi_a+\chi_b)} e^{i\pi n} & \sin^2\phi e^{i\chi_b} \\ -2i\sin\phi\cos\phi e^{\frac{i}{2}(\chi_a-\chi_b)} e^{i\pi n} & i(2-3\sin^2\phi) & 2i\sin\phi\cos\phi e^{-\frac{i}{2}(\chi_a-\chi_b)} e^{-i\pi n} \\ -\sin^2\phi e^{-i\chi_b} & 2\sin\phi\cos\phi e^{-\frac{i}{2}(\chi_a+\chi_b)} e^{-i\pi n} & -2\cos^2\phi e^{-i\chi_a} \end{pmatrix}. \quad (\text{B2})$$

Now we have $(\text{Det } U_{\text{odd}})^* = \text{Det}(-U_{\text{odd}}) = -\text{Det } U_{\text{odd}}$, and $\text{Det } U_{\text{odd}} = \mp i$ is purely imaginary (as can be directly checked with the above matrix expression). As a consequence, U_{odd} does not belong to $\text{SU}(3)$. Alternatively, $\text{SU}(3)$ matrices breaking time-reversal invariance ($\Theta U \Theta^{-1} \neq U$) cannot be odd. This result holds true for any unitary $N \times N$ matrix which is odd under time reversal provided N is odd. Indeed, $(\text{Det } U_{\text{odd}})^* = \text{Det}(-U_{\text{odd}}) = (-1)^N \text{Det } U_{\text{odd}}$ shows

that $\text{Det } U_{\text{odd}}$ is purely imaginary when N is odd. Thus U_{odd} cannot belong to $\text{SU}(N)$, and $\text{SU}(N)$ matrices breaking time-reversal invariance cannot be odd when N is odd. When N is even, U_{odd} is unimodular. This means that it is possible to have $\text{SU}(N)$ matrices which are odd under time reversal when N is even, with the notable exception of $N = 2$, as shown in the paper.

-
- [1] M. Lewenstein, A. Sanpera, V. Ahufinger, B. Damski, A. S. De, and U. Sen, *Adv. Phys.* **56**, 243 (2007).
- [2] I. Bloch, J. Dalibard, and W. Zwerger, *Rev. Mod. Phys.* **80**, 885 (2008).
- [3] W. Ketterle and M. W. Zwierlein, in *Ultra-Cold Fermi Gases*, Proceedings of the International School of Physics Enrico Fermi, Varenna, 20–30 June 2006, Course CLXIV, edited by M. Inguscio, W. Ketterle and C. Salomon (IOS Press, Amsterdam, 2007), p. 95.
- [4] Y.-J. Lin, R. L. Compton, A. R. Perry, W. D. Phillips, J. V. Porto, and I. B. Spielman, *Phys. Rev. Lett.* **102**, 130401 (2009).
- [5] Y.-J. Lin, R. L. Compton, K. Jiménez-García, J. V. Porto, and I. B. Spielman, *Nature (London)* **462**, 628 (2009).
- [6] Y.-J. Lin, K. Jiménez-García, and I. B. Spielman, *Nature (London)* **471**, 83 (2011).
- [7] P. Wang, Z.-Q. Yu, Z. Fu, J. Miao, L. Huang, S. Chai, H. Zhai, and J. Zhang, *Phys. Rev. Lett.* **109**, 095301 (2012).
- [8] L. W. Cheuk, A. T. Sommer, Z. Hadzibabic, T. Yefsah, W. S. Bakr, and M. W. Zwierlein, *Phys. Rev. Lett.* **109**, 095302 (2012).
- [9] J. Struck, C. Ölschläger, M. Weinberg, P. Hauke, J. Simonet, A. Eckardt, M. Lewenstein, K. Sengstock, and P. Windpassinger, *Phys. Rev. Lett.* **108**, 225304 (2012).
- [10] K. Jiménez-García, L. J. LeBlanc, R. A. Williams, M. C. Beeler, A. R. Perry, and I. B. Spielman, *Phys. Rev. Lett.* **108**, 225303 (2012).
- [11] E. J. Bergholtz and Z. Liu, *Int. J. Mod. Phys. B* **27**, 1330017 (2013).
- [12] N. R. Cooper and J. Dalibard, *Phys. Rev. Lett.* **110**, 185301 (2013).
- [13] N. Y. Yao, A. V. Gorshkov, C. R. Laumann, A. M. Läuchli, J. Ye, and M. D. Lukin, *Phys. Rev. Lett.* **110**, 185302 (2013).
- [14] V. Pietilä and M. Möttönen, *Phys. Rev. Lett.* **102**, 080403 (2009).
- [15] N. Goldman, D. F. Urban, and D. Bercioux, *Phys. Rev. A* **83**, 063601 (2011).
- [16] Y.-X. Hu, C. Miniatura, and B. Grémaud, *Phys. Rev. A* **92**, 033615 (2015).
- [17] N. Goldman, J. C. Budich, and P. Zoller, *Nat. Phys.* **12**, 639 (2016).
- [18] H. Zhai, *Rep. Prog. Phys.* **78**, 26001 (2015).
- [19] Y. Kawaguchi and M. Ueda, *Phys. Rep.* **520**, 253 (2012).
- [20] M. Burrello and A. Trombettoni, *Phys. Rev. Lett.* **105**, 125304 (2010).
- [21] Y. Nishida and S. Tan, *Phys. Rev. Lett.* **101**, 170401 (2008).
- [22] Y. Nishida, *Phys. Rev. A* **82**, 011605(R) (2010).
- [23] G. Lamporesi, J. Catani, G. Barontini, Y. Nishida, M. Inguscio, and F. Minardi, *Phys. Rev. Lett.* **104**, 153202 (2010).
- [24] W.-M. Huang, K. Irwin, and S.-W. Tsai, *Phys. Rev. A* **87**, 031603(R) (2013).
- [25] M. Iskin and A. L. Subasi, *Phys. Rev. A* **82**, 063628 (2010).
- [26] L. F. Livi, G. Cappellini, M. Diem, L. Franchi, C. Clivati, M. Frittelli, F. Levi, D. Calonico, J. Catani, M. Inguscio, and L. Fallani, *Phys. Rev. Lett.* **117**, 220401 (2016).
- [27] C. Gross and I. Bloch, *Science* **357**, 995 (2017).
- [28] S. Sugawa, F. Salces-Carcoba, A. R. Perry, Y. Yue, and I. B. Spielman, *Science* **360**, 1429 (2018).
- [29] M. W. Ray, E. Ruokokoski, S. Kandel, M. Möttönen, and D. S. Hall, *Nature (London)* **505**, 657 (2014).
- [30] J. Dalibard, F. Gerbier, G. Juzeliūnas, and P. Öhberg, *Rev. Mod. Phys.* **83**, 1523 (2011).
- [31] N. Goldman, G. Juzeliūnas, P. Öhberg, and I. B. Spielman, *Rep. Prog. Phys.* **77**, 126401 (2014).
- [32] W. S. Cole, S. Zhang, A. Paramakanti, and N. Trivedi, *Phys. Rev. Lett.* **109**, 085302 (2012).
- [33] D. Cocks, P. P. Orth, S. Rachel, M. Buchhold, K. Le Hur, and W. Hofstetter, *Phys. Rev. Lett.* **109**, 205303 (2012), and references therein.
- [34] N. Goldman, A. Kubasiak, P. Gaspard, and M. Lewenstein, *Phys. Rev. A* **79**, 023624 (2009).
- [35] Z. Cai, X. Zhou, and C. Wu, *Phys. Rev. A* **85**, 061605(R) (2012).
- [36] J. Radić, A. Di Ciolo, K. Sun, and V. Galitski, *Phys. Rev. Lett.* **109**, 085303 (2012).
- [37] M. Sato, Y. Takahashi, and S. Fujimoto, *Phys. Rev. Lett.* **103**, 020401 (2009).

- [38] N. Goldman, W. Beugeling, and C. Morais-Smith, *Europhys. Lett.* **97**, 23003 (2012).
- [39] J. Minář and B. Grémaud, *Phys. Rev. B* **88**, 235130 (2013).
- [40] J. P. Vyasnakere, S. Zhang, and V. B. Shenoy, *Phys. Rev. B* **84**, 014512 (2011).
- [41] L. Han and C. A. R. Sá de Melo, *Phys. Rev. A* **85**, 011606(R) (2012).
- [42] A. Kubasiak, P. Massignan, and M. Lewenstein, *Europhys. Lett.* **92**, 46004 (2010).
- [43] M. Iskin and A. L. Subasi, *Phys. Rev. A* **84**, 043621 (2011).
- [44] M. Iskin and A. L. Subasi, *Phys. Rev. A* **87**, 063627 (2013).
- [45] M. Iskin, *Phys. Rev. A* **88**, 013631 (2013).
- [46] K. Riedl, C. Drukier, P. Zalom, and P. Kopietz, *Phys. Rev. A* **87**, 063626 (2013).
- [47] Y.-X. Hu, Ch. Miniatura, D. Wilkowski, and B. Grémaud, *Phys. Rev. A* **90**, 023601 (2014).
- [48] A. Kosior and K. Sacha, *Europhys. Lett.* **107**, 26006 (2014).
- [49] R. Barnett, G. R. Boyd, and V. Galitski, *Phys. Rev. Lett.* **109**, 235308 (2012).
- [50] I. Mandal and A. Bhattacharya, *Condens. Matter* **1**, 2 (2016).
- [51] W. Han, X.-F. Zhang, S.-W. Song, H. Saito, W. Zhang, W.-M. Liu, and S.-G. Zhang, *Phys. Rev. A* **94**, 033629 (2016).
- [52] T. Graß, R. W. Chhajlany, C. A. Muschik, and M. Lewenstein, *Phys. Rev. B* **90**, 195127 (2014).
- [53] G. Go, J.-H. Park, and J. H. Han, *Phys. Rev. B* **87**, 155112 (2013).
- [54] *Quantum Hall Effects*, edited by Z. F. Ezawa (World Scientific, Singapore, 2013).
- [55] Y. Li, P. Sengupta, G. G. Batrouni, C. Miniatura, and B. Grémaud, *Phys. Rev. A* **92**, 043605 (2015).
- [56] R. Resta, *J. Phys.: Condens. Matter* **12**, R107 (2000).
- [57] J. Asbóth, L. Oroszlány, and A. Pály, *A Short Course on Topological Insulators*, Lecture Notes in Physics, Vol. 919 (Springer, 2016).
- [58] D. Xiao, M.-Ch. Chang, and Q. Niu, *Rev. Mod. Phys.* **82**, 1959 (2010).
- [59] *Topological Aspects of Condensed Matter Physics*, Les Houches Summer School Session CIII, edited by C. Chamon, M. O. Goerbig, R. Moessner, and L. F. Cugliandolo (Oxford University Press, Oxford, UK, 2017).
- [60] Y. Hatsugai, *Phys. Rev. Lett.* **71**, 3697 (1993).
- [61] Y. Hatsugai, *Phys. Rev. B* **48**, 11851 (1993).
- [62] Y. Hatsugai, *J. Phys.: Condens. Matter* **9**, 2507 (1997).
- [63] C. L. Kane and E. J. Mele, *Phys. Rev. Lett.* **95**, 146802 (2005).
- [64] M. Z. Hasan and C. L. Kane, *Rev. Mod. Phys.* **84**, 3045 (2010).
- [65] C. Chiu, J. C. Y. Teo, A. P. Schnyder, and S. Ryu, *Rev. Mod. Phys.* **88**, 35005 (2016).
- [66] S. Ryu, A. P. Schnyder, A. Furusaki, and A. W. W. Ludwig, *New J. Phys.* **12**, 065010 (2010).
- [67] *Modern Quantum Mechanics*, revised edition, edited by J. J. Sakurai and San Fu Tuan (Pearson Education, London, 1994).
- [68] *Topological Insulators and Topological Superconductors*, B. A. Bernevig with T. L. Taylor (Princeton University Press, Princeton, NJ, 2013).
- [69] A. Bermudez, N. Goldman, A. Kubasiak, M. Lewenstein, and M. A. Martin-Delgado, *New J. Phys.* **12**, 033041 (2010).
- [70] Triple degeneracies cannot occur because $N_{\mathbf{k}}^\dagger N_{\mathbf{k}}$ is never diagonal in the Brillouin zone, as can be checked by direct inspection.
- [71] J. N. Fuchs, F. Piéchon, M. O. Goerbig, and G. Montambaux, *Eur. Phys. J. B* **77**, 351 (2010).
- [72] Noting that $P\mathcal{H}_{\mathbf{k}}(\Delta)P = -\mathcal{H}_{\mathbf{k}}(-\Delta)$, we also infer that $C_n(\Delta) = C_n(-\Delta)$.
- [73] T. Fukui, Y. Hatsugai, and H. Suzuki, *J. Phys. Soc. Jpn.* **74**, 1674 (2005).
- [74] Interestingly, the numerical method described in Ref. [73] yields the same values for the Chern numbers at the middle bands C_3 and C_4 when $\Delta = 0$, though strictly speaking, these Chern numbers are not defined in the absence of the mass imbalance term since the two middle bands touch each other. The equality $C_3 = C_4$ inferred from the mirror symmetry of the spectrum, when bands are isolated, is maintained somehow down to $\Delta = 0$.
- [75] A. H. Castro Neto, N. M. R. Peres, K. S. Novoselov, and A. K. Geim, *Rev. Mod. Phys.* **81**, 109 (2009).